FCS-MPC-Based Fault-Tolerant Control of Five-Phase IPMSM for MTPA Operation

Guohai Liu, *Senior Member, IEEE*, Chengyan Song, and Qian Chen, *Member, IEEE*

***Abstract*—This article proposes a new fault-tolerant control strategy based on finite-control-set model predictive control (FCS-MPC) for interior permanent-magnet synchronous motor (IPMSM) drives under open-circuit faults, including single-phase and double-phase faults. In particular, the double-phase fault will cause a big disturbance to the performance of the motor, but there is no research focused on it with FCS-MPC. The key of this method is that a z subspace orthogonal to the fundamental space is proposed to reduce the total current harmonic distortions under the single-phase fault. And the distributions of space voltage vectors under a double-phase fault are established to realize the fault-tolerant operation. On the other hand, most of the research is focused on the fault-tolerant control of $i_d = 0$, which is not suitable for the IPMSM, due to the ignorance of the reluctance torque. Hence, the proposed strategy is extended into the maximum torque per ampere operation by virtual signal injection, then the amplitudes of phase currents can be reduced and the efficiency of the system can be improved under fault conditions. Compared with the existing fault-tolerant control schemes, the proposed strategy can realize the fault-tolerant operation under open-circuit faults with faster control response and higher operation efficiency, which has been validated by experimental results.**

***Index Terms*—Fault tolerant, finite control set, maximum torque per ampere (MPTA), model predictive control, virtual signal injection control (VSIC).**

I. Introduction

As AN extended case example of multiphase drives, the five-phase interior permanent-magnet synchronous motor (IPMSM) has been widely used in a variety of industrial applications due to its high power density, high efficiency, high torque production, and wide speed operating range [1]–[3]. Besides, with the increased safety and reliability requirements in these areas, the postfault control strategies for multiphase drives have attracted more and more attentions.

Regarding the traditional control methods, the field-oriented control (FOC) [4]–[7] and direct torque control (DTC) [8]–[13] have been extended into multiphase motor drives to realize the fault-tolerant control. Besides, to improve the performance, proportional-resonant control [14], current references control [15], [16], sliding mode control [17], [18], and so on, are also been constructed to the fault-tolerant operation. With the development of high-performance control, finite-control-set model predictive control (FCS-MPC) has become an interesting alternative to the traditional control methods in the multiphase drives, due to its intuitive control structure, the fast response, and flexibility [19]–[21]. It takes into account the discrete nature of power converters, and uses a single cost function to solve the online optimization problem without an external modulator [22]. The optimal switching vector that minimizes the cost function is selected as the output of the controller to fulfill the current requirements. In addition, the design of a specific cost function with adjustable weight factors can easily represent the considered variables and control objectives of the system [23]. As for multiphase motors, the stator current can be severely distorted due to the multiharmonic subspace. Therefore, the control algorithm should be designed according to its own particularity and application requirements. The FCS-MPC was first developed for multiphase phase systems in [24] and [25], and then, many contributions have been made in the last decades [26], [27]. These works proved the capability of the FCS-MPC strategy to regulate multiphase motors using different number of switching states and model approaches.

Recently, the FSC-MPC has been introduced into fault-tolerant control for multiphase drives, e.g., six-phase and five-phase motors [28]–[35]. In [28]–[32], different control strategies were proposed to realize the fault-tolerant operation for the six-phase motor, including the pulsewidth modulation, remedial control without controller structure reconfiguration, virtual voltage vectors, and so on. In [33] and [34], a fault-tolerant FSC-MPC was proposed for the five-phase induction motor system, including single-phase fault and insulated-gate bipolar transistor (IGBT)-gating fault, but the orthogonality of the reduced-order transformation matrix under the fault condition is not guaranteed, which will result in coupling currents. In [35], a fault-tolerant FSC-MPC with duty cycle optimization was proposed to improve the performance of the five-phase flux-switching motor drive under a single-phase fault, but no ideal results were obtained due to the large harmonics in currents. In general, although the existing methods with the FCS-MPC are focused on the fault-tolerant operation of the five-phase motor under a single-phase fault, a series of problems still exist such as serious current distortion and complex calculation.

Manuscript received January 21, 2019; revised May 23, 2019; accepted July 24, 2019. Date of publication July 28, 2019; date of current version December 13, 2019. This work was supported in part by National Natural Science Foundation of China under Grants 51877098 and 51707083, and in part by Priority Academic Program Development of Jiangsu Higher Education Institutions. Recommended for publication by Associate Editor H. Hofmann. *(Corresponding author: Qian Chen.)*

The authors are with the School of Electrical and Information Engineering, Jiangsu University, Zhenjiang 212013, China, and also with Jiangsu Key Laboratory of Drive and Intelligent Control for Electric Vehicle, Zhenjiang 212013, China (e-mail: ghliu@ujs.edu.cn; scy0910@qq.com; chenqian0501@ujs.edu.cn).

Color versions of one or more of the figures in this article are available online at http://ieeexplore.ieee.org

Digital Object Identifier 10.1109/TPEL.2019.2931712

Also, they are not suitable for the double-phase fault due to the lack of more freedom. However, with the research of the fault-tolerant multiphase motor, the single-phase fault may not affect the normal operation of the motor, and the double-phase fault will still cause a big disturbance to the performance of the motor. Hence, it is of great significance to study the double-phase fault for the multiphase motor. Many control methods have been extended into a double-phase fault of a five-phase motor [15], [16], [18], but there is no literature about the FCS-MPC.

On the other hand, the most of research is focused on the fault-tolerant control of $i_d = 0$, which is not suitable for the IPMSM, due to the ignorance of the reluctance torque. To achieve optimal efficiency, the maximum torque per ampere (MTPA) control is often used for the IPMSM [36]–[41]. In these MTPA methods, a new virtual signal injection (VSIC) MTPA control was proposed in [40]. Compared with the other MTPA approaches, the obvious advantage of this method is no additional iron loss and copper loss due to no real signal injection. Then, the MTPA method was extended into fault-tolerant operation for the IPMSM [41]. Although the amplitudes of phase currents are reduced and the efficiency is improved, the postfault strategy is only realized by the FOC, and there is no research focused on the MTPA fault-tolerant operation with the FCS-MPC, which has a superior performance compared with the FOC [21].

This article proposes a novel fault-tolerant control strategy based on the FCS-MPC for five-phase IPMSM drives under open-circuit faults. A z subspace orthogonal to the fundamental space is proposed to reduce the current total harmonic distortions under a single-phase fault. And the postfault space voltage vector diagrams are reconstructed to realize the fault-tolerant control under a double-phase fault. Furthermore, the combination of the VSIC-based MTPA scheme with the FSC-MPC-based fault-tolerant control can improve the performances of the system effectively. This article is organized as follows: the five-phase IPMSM and its drive will be briefly presented in Section II. In Section III, the reduced-order matrices for fault conditions will be derived to construct the distributions of space voltage vectors. The discrete models of a five-phase inverter system under open-circuit faults will be described, and the basic concept of the FCS-MPC algorithm will be presented in Section IV. Section V will introduce the fault-tolerant control for MTPA operation in the IPMSM. Section VI will verify the algorithm by experimental results. Finally, conclusions will be summarized in Section VII.

II. Motor Description and Inverter Model

The five-phase 40-slot and 8-pole IPMSM prototype is shown in Fig. 1(a), which is designed for electric vehicles with one or two passengers. The single-layer integral-slot distribution winding and the shifted asymmetrical rotor poles were employed to reduce the 9th and 11th harmonics, resulting in a low torque ripple [42]. Fig. 1(b) shows the corresponding fast Fourier transform result of back-EMF waveform at rated speed 1500 r/min. The fast Fourier transform result shows that the third harmonic content of the back-EMF is 3.5%, the fifth harmonic content is 14.6%, the seventh harmonic content is 4.5%, and the ninth harmonic content is 1.7%. Although the fifth harmonic is the main back-EMF harmonic of this motor, it does not result the torque ripple for the fault-tolerant control of the motor with star-type connection. Besides, the third harmonic, seventh harmonic, and ninth harmonic are small and can be ignored. Hence, only the fundamental component needs to be considered in the synchronous-frame model of this five-phase IPMSM.

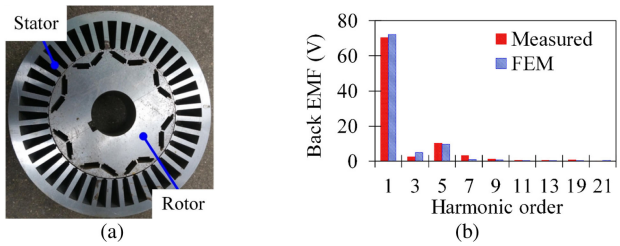

Fig. 1. Five-phase IPMSM. (a) Prototype. (b) Harmonic order of back-EMF.

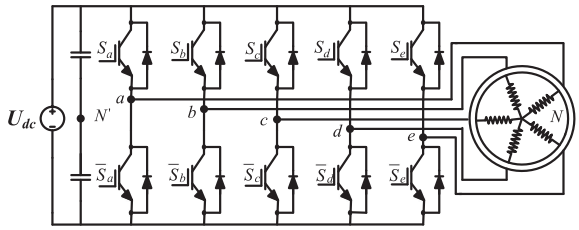

Fig. 2. Five-phase IPMSM and its inverter drive.

The star-type connection of the half bridge structure is adopted in the inverter topology of the five-phase IPMSM drive system, as shown in Fig. 2. Voltages of the inverter at the phase coordinate are described as (1) under normal condition. Besides, the five-phase voltages composed to be zero as a general principle is expressed as (2).

$$\begin{cases} U_a = U_{aN'} + U_{N'N} = \dfrac{U_{\rm dc}}{2}(2S_a - 1) + U_{N'N} \\ U_b = U_{bN'} + U_{N'N} = \dfrac{U_{\rm dc}}{2}(2S_b - 1) + U_{N'N} \\ U_c = U_{cN'} + U_{N'N} = \dfrac{U_{\rm dc}}{2}(2S_c - 1) + U_{N'N} \\ U_d = U_{dN'} + U_{N'N} = \dfrac{U_{\rm dc}}{2}(2S_d - 1) + U_{N'N} \\ U_e = U_{eN'} + U_{N'N} = \dfrac{U_{\rm dc}}{2}(2S_e - 1) + U_{N'N} \end{cases} \tag{1}$$

$$U_a + U_b + U_c + U_d + U_e = 0 \tag{2}$$

where $U_{\rm dc}$ is the dc line voltage; $U_x (x = a, b, c, d, e)$ is the five-phase voltage; $U_{xN\prime} (x = a, b, c, d, e)$ is voltage between the inverter output and the bus central point; $U_{N'N}$ is the voltage between bus neutral point and motor neutral point; and $S_x (x = a, b, c, d, e)$ represents switch status of each bridge arm, where "1" indicates the upper switch is ON, while "0" indicates the lower switch is ON.

III. Modeling Under Open-Circuit Fault

For a multiphase motor, the single-phase and double-phase faults are common phenomenon. In this article, the phase-A open-circuit fault and phases C and D as well as phases-B and -E double-phase faults are analyzed.

A. Single-Phase Open-Circuit Fault

Assuming that a single-phase fault happens on the phase A, the current of the phase A equals zero. In order to maintain a constant magnetomotive force as same as that in normal operation and maximize the torque production, the remaining healthy phase currents have to be regulated by applying the constraint of the equal magnitudes. The phase currents can be calculated as [5]

$$I_s = \begin{bmatrix} I_b \\ I_c \\ I_d \\ I_e \end{bmatrix} = 1.382 \begin{bmatrix} \cos(0.5\alpha) & \sin(0.5\alpha) \\ \cos(2\alpha) & \sin(2\alpha) \\ \cos(3\alpha) & \sin(3\alpha) \\ \cos(4.5\alpha) & \sin(4.5\alpha) \end{bmatrix} \begin{bmatrix} \cos\theta & -\sin\theta \\ \sin\theta & \cos\theta \end{bmatrix} \begin{bmatrix} i_d \\ i_q \end{bmatrix} \tag{3}$$

where $\alpha = 0.4\pi$; θ is the electrical angle; $I_x (x = a, b, c, d, e)$ is the phase current; and i_d and i_q are currents in *d–q* axes.

It can be noted from (3) that the currents under the fault-tolerant condition are different from that under the normal condition. Therefore, in order to eliminate the coupling current and realize the fault-tolerant operation, the transformation matrices have to be redefined. According to [6], the new Clarke transformation matrix can be derived as (4) shown at the bottom of this page, and the Park matrix can be expressed as

$$T^1_{\text{Park}} = \begin{bmatrix} \cos\theta & \sin\theta & 0 & 0 \\ -\sin\theta & \cos\theta & 0 & 0 \\ 0 & 0 & 1 & 0 \\ 0 & 0 & 0 & 1 \end{bmatrix}. \tag{5}$$

Although the phase A is open circuit, the induced EMF is still existed. From Fig. 2, the phase voltages under the fault condition can be expressed as

$$\begin{bmatrix} U_b \\ U_c \\ U_d \\ U_e \end{bmatrix} = U_{\text{dc}} \begin{bmatrix} 1\,0\,0\,0 \\ 0\,1\,0\,0 \\ 0\,0\,1\,0 \\ 0\,0\,0\,1 \end{bmatrix} \begin{bmatrix} S_b \\ S_c \\ S_d \\ S_e \end{bmatrix} - \left(\frac{U_{\text{dc}}}{2} + U_{NN'} \right) \begin{bmatrix} 1 \\ 1 \\ 1 \\ 1 \end{bmatrix}. \tag{6}$$

TABLE I
Switching Vectors Under Single-Phase Fault in α–β Frame

Voltage vector	Amplitude	S_b, S_c, S_d, S_e
$\boldsymbol{U}_{15}$, $\boldsymbol{U}_0$, $\boldsymbol{U}_{10}$, $\boldsymbol{U}_5$	0	1111, 0000, 1010, 0101
$\boldsymbol{U}_8$, $\boldsymbol{U}_{13}$, $\boldsymbol{U}_4$, $\boldsymbol{U}_{14}$	$0.3804U_{\text{dc}}$	1000, 1101, 0100, 1110
$\boldsymbol{U}_2$, $\boldsymbol{U}_7$, $\boldsymbol{U}_1$, $\boldsymbol{U}_{11}$		0010, 0111, 0001, 1011
$\boldsymbol{U}_6$, $\boldsymbol{U}_9$	$0.4472U_{\text{dc}}$	0110, 1001
$\boldsymbol{U}_3$, $\boldsymbol{U}_{12}$	$0.6145U_{\text{dc}}$	0011, 1100

TABLE II
Switching Vectors Under Single-Phase Fault in z Frame

Voltage vector	Amplitude	S_b, S_c, S_d, S_e
$\boldsymbol{U}_0$, $\boldsymbol{U}_3$, $\boldsymbol{U}_6$	0	0000, 0011, 0110
$\boldsymbol{U}_9$, $\boldsymbol{U}_{12}$, $\boldsymbol{U}_{15}$		1001, 1100, 1111
$\boldsymbol{U}_1$, $\boldsymbol{U}_4$, $\boldsymbol{U}_7$, $\boldsymbol{U}_{13}$	$0.1902U_{\text{dc}}$	0001, 0100, 0111, 1101
$\boldsymbol{U}_2$, $\boldsymbol{U}_8$, $\boldsymbol{U}_{11}$, $\boldsymbol{U}_{14}$		0010, 1000, 1011, 1110
$\boldsymbol{U}_5$, $\boldsymbol{U}_{10}$	$0.3804U_{\text{dc}}$	0101, 1010

Substituting (2) into (6), the following equation can be obtained:

$$\left(U_{NN'} + \frac{U_{\text{dc}}}{2} \right) = \frac{U_{\text{dc}}}{4}(S_b + S_c + S_d + S_e) + \frac{1}{4}U_a. \tag{7}$$

With the Clarke transformation matrix from the standard coordinate *a–b–c–d–e* to the static frame, the voltages in α–β frame and z frame can be obtained as

$$\begin{bmatrix} u_\alpha \\ u_\beta \\ u_z \end{bmatrix} = T^A_{\text{Clarke}} \begin{bmatrix} U_b \\ U_c \\ U_d \\ U_e \end{bmatrix} = \begin{bmatrix} 0.2236U_{\text{dc}}(S_b - S_c - S_d + S_e) \\ 0.3077U_{\text{dc}}(S_b + S_c - S_d - S_e) \\ 0.1902U_{\text{dc}}(S_b - S_c + S_d - S_e) \end{bmatrix}. \tag{8}$$

Furthermore, taking the switching function of the inverter into (8), the distributions of space voltage vectors in the α–β frame and z frame are depicted in Tables I and II, respectively. Also, the corresponding distribution diagrams are shown in Fig. 3. Although the amplitudes of the switching vectors U_5 and U_{10} are zero, they are not really zero switching vectors due to the switch sign of two vectors. Hence, they are abandoned in the selection of switching vectors. On the other hand, considering the switching vectors U_8 and U_{13}, U_4 and U_{14}, U_2 and U_7, *and* U_1 and U_{11} have the same effect, respectively. In order to reduce the inverter switching frequency and amount of computation, U_8, U_4, U_2, U_1, U_9, U_{12}, U_6, and U_3 are chosen as effective vectors.

$$T^A_{\text{Clarke}} = \begin{bmatrix} \cos 0.5\alpha/3.618 & \cos 2\alpha/3.618 & \cos 3\alpha/3.618 & \cos 4.5\alpha/3.618 \\ \sin 0.5\alpha/1.91 & \sin 2\alpha/1.91 & \sin 3\alpha/1.91 & \sin 4.5\alpha/1.91 \\ \sin\alpha/5 & \sin 4\alpha/5 & \sin 6\alpha/5 & \sin 9\alpha/5 \\ 1 & 1 & 1 & 1 \end{bmatrix} \tag{4}$$

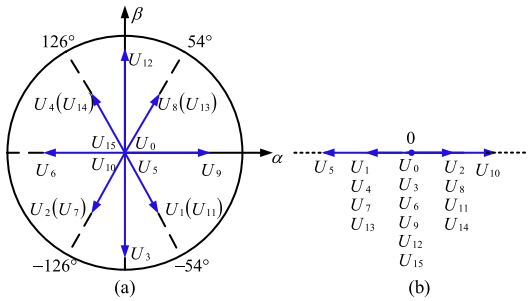

Fig. 3. Space voltage vectors diagrams (single-phase fault). (a) α–β space voltage vectors. (b) z space voltage vectors.

B. Double-Phase Open-Circuit Fault

For the five-phase motor, two kinds of double-phase faults may occur, i.e., adjacent phase and nonadjacent phase. The modeling principles under the aforementioned two fault conditions are similar.

1) Adjacent-Phase Open-Circuit Fault: Assuming open-circuit fault happens on phases C and D, in order to maintain constant magnetomotive force as same as that in normal operation and maximize the torque production, the phase currents can be calculated as [5]

$$I_s = \begin{bmatrix} I_a \\ I_b \\ I_e \end{bmatrix} = \begin{bmatrix} 3.618 & 0 \\ 2.236\cos\alpha_1 & 2.236\sin\alpha_1 \\ 2.236\cos\alpha_1 & -2.236\sin\alpha_1 \end{bmatrix} \begin{bmatrix} \cos\theta & -\sin\theta \\ \sin\theta & \cos\theta \end{bmatrix} \begin{bmatrix} i_d \\ i_q \end{bmatrix} \tag{9}$$

where $\alpha_1 = 0.8\,\pi$.

And the new Clarke and Park transformation matrices can be derived as

$$T^{CD}_{\text{Clarke}} = \frac{2}{5}\begin{bmatrix} 1+\frac{2}{3}\cos 2\alpha & \cos\alpha+\frac{2}{3}\cos 2\alpha & \cos 4\alpha+\frac{2}{3}\cos 2\alpha \\ 0 & \sin\alpha & \sin 4\alpha \\ 1 & 1 & 1 \end{bmatrix} \tag{10}$$

$$T^{2}_{\text{Park}} = \begin{bmatrix} \cos\theta & \sin\theta & 0 \\ -\sin\theta & \cos\theta & 0 \\ 0 & 0 & 1 \end{bmatrix}. \tag{11}$$

The phase voltages under the fault condition can be expressed as

$$\begin{bmatrix} U_a \\ U_b \\ U_e \end{bmatrix} = U_{\text{dc}} \begin{bmatrix} 1 & 0 & 0 \\ 0 & 1 & 0 \\ 0 & 0 & 1 \end{bmatrix} \begin{bmatrix} S_a \\ S_b \\ S_e \end{bmatrix} - \left(\frac{U_{\text{dc}}}{2} + U_{NN'}\right) \begin{bmatrix} 1 \\ 1 \\ 1 \end{bmatrix}. \tag{12}$$

Substituting (2) into (12), the following equation can be obtained:

$$\left(U_{NN'} + \frac{U_{\text{dc}}}{2}\right) = \frac{U_{\text{dc}}}{3}(S_a + S_b + S_e) + \frac{1}{3}(U_c + U_d). \tag{13}$$

TABLE III
SWITCHING VECTORS UNDER ADJACENT-PHASE FAULT

Voltage vector	Amplitude	S_a, S_b, S_e
$\boldsymbol{U}_7$, $\boldsymbol{U}_0$	0	111, 000
$\boldsymbol{U}_1$, $\boldsymbol{U}_2$, $\boldsymbol{U}_5$, $\boldsymbol{U}_6$	$0.3915U_{\text{dc}}$	001, 010, 101, 110
$\boldsymbol{U}_3$, $\boldsymbol{U}_4$	$0.1840U_{\text{dc}}$	011, 100

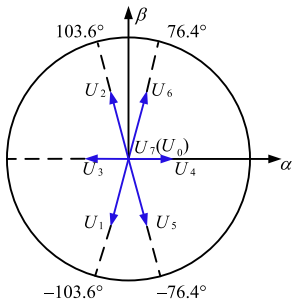

Fig. 4. Space voltage vectors diagram (adjacent-phase fault).

With the Clarke transformation matrix from the standard coordinate *a*–*b*–*c*–*d*–*e* to the static frame, the voltages in α–β frame can be obtained as

$$\begin{bmatrix} U_\alpha \\ U_\beta \end{bmatrix} = T^{CD}_{\text{Clarke}} \begin{bmatrix} U_a \\ U_b \\ U_e \end{bmatrix} = \begin{bmatrix} 0.0920U_{\text{dc}}(2S_a - S_b - S_e) \\ 0.3805U_{\text{dc}}(S_b - S_e) \end{bmatrix}. \tag{14}$$

Furthermore, taking the switching function of the inverter into (8), the distribution of space voltage vectors in the α–β frame is depicted in Table III. Also, the corresponding distribution diagram in the α–β frame is shown in Fig. 4.

2) Nonadjacent-Phase Open-Circuit Fault: Similarly, assuming open-circuit fault happens on the phases B and E, the phase currents can be calculated as [5]

$$I_s = \begin{bmatrix} I_a \\ I_c \\ I_d \end{bmatrix} = \begin{bmatrix} 1.382 & 0 \\ 2.236\cos\alpha_2 & 2.236\sin\alpha_2 \\ 2.236\cos\alpha_2 & -2.236\sin\alpha_2 \end{bmatrix} \begin{bmatrix} \cos\theta & -\sin\theta \\ \sin\theta & \cos\theta \end{bmatrix} \begin{bmatrix} i_q \\ i_d \end{bmatrix} \tag{15}$$

where $\alpha_2 = 0.6\,\pi$.

And the new Clarke and Park transformation matrices can be derived as

$$T^{\text{BE}}_{\text{Clarke}} = \frac{2}{5}\begin{bmatrix} 1+\frac{2}{3}\cos\alpha & \cos 2\alpha+\frac{2}{3}\cos\alpha & \cos 3\alpha+\frac{2}{3}\cos\alpha \\ 0 & \sin 2\alpha & \sin 3\alpha \\ 1 & 1 & 1 \end{bmatrix} \tag{16}$$

$$T^{2}_{\text{Park}} = \begin{bmatrix} \cos\theta & \sin\theta & 0 \\ -\sin\theta & \cos\theta & 0 \\ 0 & 0 & 1 \end{bmatrix}. \tag{17}$$

TABLE IV
SWITCHING VECTORS UNDER NONADJACENT-PHASE FAULT

Voltage vector	Amplitude	S_a, S_c, S_d
$\boldsymbol{U}_7, \boldsymbol{U}_0$	0	111, 000
$\boldsymbol{U}_1, \boldsymbol{U}_2, \boldsymbol{U}_5, \boldsymbol{U}_6$	$0.3368U_{\rm dc}$	001, 010, 101, 110
$\boldsymbol{U}_3, \boldsymbol{U}_4$	$0.4822U_{\rm dc}$	011, 100

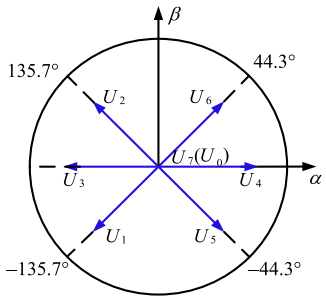

Fig. 5. Space voltage vectors diagram (nonadjacent-phase fault).

The phase voltages under the fault condition can be expressed

$$\begin{bmatrix} U_a \\ U_c \\ U_d \end{bmatrix} = U_{\rm dc} \begin{bmatrix} 1 & 0 & 0 \\ 0 & 1 & 0 \\ 0 & 0 & 1 \end{bmatrix} \begin{bmatrix} S_a \\ S_c \\ S_d \end{bmatrix} - \left(\frac{U_{\rm dc}}{2} + U_{NN'} \right) \begin{bmatrix} 1 \\ 1 \\ 1 \end{bmatrix}. \tag{18}$$

Substituting (2) into (18), the following equation can be obtained:

$$\left(U_{NN'} + \frac{U_{\rm dc}}{2} \right) = \frac{U_{\rm dc}}{3}(S_a + S_c + S_d) + \frac{1}{3}(U_b + U_e). \tag{19}$$

With the Clarke transformation matrix from the standard coordinate *a–b–c–d–e* to the static frame, the voltages in α–β frame can be obtained as

$$\begin{bmatrix} U_\alpha \\ U_\beta \end{bmatrix} = T^{\rm BE}_{\rm Clarke} \begin{bmatrix} U_a \\ U_c \\ U_d \end{bmatrix} \begin{bmatrix} 0.2411U_{\rm dc}(2S_a - S_c - S_d) \\ 0.2352U_{\rm dc}(S_c - S_d) \end{bmatrix}. \tag{20}$$

Furthermore, taking the switching function of the inverter into (8), the distribution of space voltage vectors in the α–β frame is depicted in Table IV. Also, the corresponding distribution diagram in the α–β frame is shown in Fig. 5.

IV. FCS-MPC-BASED FAULT-TOLERANT CONTROL

A. Prediction Model Under Single-Phase Open-Circuit Fault

The stator voltage equation under the phase-A open-circuit fault can be calculated as

$$U_{s1} = R_s I_{s1} + \frac{d}{dt}\left(L_s I_{s1} + \varphi^A_{s1} \right) \tag{21}$$

where

$$\varphi^A_{s1} = \begin{bmatrix} \varphi_b \\ \varphi_c \\ \varphi_d \\ \varphi_e \end{bmatrix} = \varphi_m \begin{bmatrix} \cos(\theta - \alpha) \\ \cos(\theta - 2\alpha) \\ \cos(\theta - 3\alpha) \\ \cos(\theta - 4\alpha) \end{bmatrix}. \tag{22}$$

The motor voltage equation on the synchronous frame can be expressed by

$$\begin{bmatrix} u_d & u_q & u_z & u_0 \end{bmatrix} = T^1_{\rm Park} T^A_{\rm Clarke} \begin{bmatrix} U_b & U_c & U_d & U_e \end{bmatrix}^T. \tag{23}$$

Substituting (4) and (5) into (23), the following equation can be obtained:

$$\begin{cases} u_d = i_d R_s + L_d \dfrac{di_d}{dt} - \omega_e L_q i_q + e_d \\ u_q = i_q R_s + L_q \dfrac{di_q}{dt} + \omega_e L_d i_d + e_q \\ u_z = i_z R_s + L_{ls} \dfrac{di_z}{dt} + e_z \\ u_0 = -e_A \end{cases} \tag{24}$$

where e_d and e_q are the fundamental *d–q* axes back-EMF, and their calculations are detailed in Appendix A; u_d and u_q are the fundamental *d–q* axes stator voltage; u_z and u_0 are third space and zero-sequence component of stator voltage, respectively; R_s is the stator resistance; L_d, L_q are the fundamental *d–q* axes inductances; L_{ls} is the leakage inductance; ω_e is the electrical rotating speed; φ_m is the fundamental permanent-magnet flux linkage; and e_A is the back-EMF of the phase A.

Applying the Euler formula to discretize the voltage equation in (24) and transforming the result into a single time step, the predictive current model can be obtained as

$$\begin{cases} i_d(k+1) = i_d(k) + \dfrac{Ts}{Ld}(u_d(k) - R_s i_d(k) \\ \qquad\qquad + \omega_e L_q i_q(k) - e_d(k)) \\ i_q(k+1) = i_q(k) + \dfrac{Ts}{Lq}(u_q(k) - R_s i_q(k) \\ \qquad\qquad - \omega_e L_d i_d(k) - e_q(k)) \\ i_z(k+1) = i_z(k) + \dfrac{Ts}{Lls}(u_z(k) - R_s i_z(k) - e_z(k)) \end{cases} \tag{25}$$

where T_s is control period; $i_d(k)$, $i_q(k)$, and $i_z(k)$ are the currents in *d–q–z* axes at the current moment; $i_d(k+1)$, $i_q(k+1)$, and $i_z(k+1)$ are the predicted current at (k+1)th instant; and $u_d(k)$, $u_q(k)$, $u_z(k)$ and $e_d(k)$, $e_q(k)$, $e_z(k)$ are stator voltage and back-EMF at the current moment, respectively.

From (25), three current error terms should be considered in the cost function, and defined as the following:

$$\begin{aligned} g_1 = {} & |i_{\rm dref} - i_d(k+1)|^2 + |i_{\rm qref} - i_q(k+1)|^2 \\ & + |i_{z\rm ref} - i_z(k+1)|^2 \end{aligned} \tag{26}$$

where $i_{\rm dref}$, $i_{\rm qref}$, and $i_{z\rm ref}$ represent the desired value of the corresponding currents in *d-*, *q-*, and *z*-axes, respectively.

B. Prediction Model Under Double-Phase Open-Circuit Fault

1) Adjacent-Phase Open-Circuit Fault: The stator voltage equation under the phases-C and -D open-circuit fault can be

calculated as

$$U_{s2} = R_s I_{s2} + \frac{d}{dt}\left(L_s I_{s2} + \varphi_{s2}^{CD}\right) \tag{27}$$

where

$$\varphi_{s2}^{CD} = \begin{bmatrix} \varphi_a \\ \varphi_b \\ \varphi_e \end{bmatrix} = \varphi_m \begin{bmatrix} \cos(\theta) \\ \cos(\theta - \alpha) \\ \cos(\theta - 4\alpha) \end{bmatrix}. \tag{28}$$

The motor voltage equation on the synchronous frame can be expressed by

$$\begin{bmatrix} u_d & u_q & u_0 \end{bmatrix} = T_{\text{Park}}^2 T_{\text{Clarke}}^{CD} \begin{bmatrix} U_a & U_b & U_e \end{bmatrix}^T. \tag{29}$$

Substituting (10) and (11) into (29), the following equation can be obtained:

$$\begin{cases} u_d = i_d R_s + L_d \dfrac{di_d}{dt} - \omega_e L_q i_q + e_d \\ u_q = i_q R_s + L_q \dfrac{di_q}{dt} + \omega_e L_d i_d + e_q \\ u_0 = -0.4(e_C + e_D) \end{cases} \tag{30}$$

where e_C and e_D are the back-EMF of the phases C and D, and the calculations of e_d and e_q are detailed in Appendix B-1.

Applying the Euler formula to discretize the voltage equation in (30) and transforming the result into a single time step, the predictive current model can be obtained as

$$\begin{cases} i_d(k+1) = i_d(k) + \dfrac{Ts}{Ld}(u_d(k) - R_s i_d(k) \\ \qquad\qquad + \omega_e L_q i_q(k) - e_d(k)) \\ i_q(k+1) = i_q(k) + \dfrac{Ts}{Lq}(u_q(k) - R_s i_q(k) \\ \qquad\qquad - \omega_e L_d i_d(k) - e_q(k)). \end{cases} \tag{31}$$

From the aforementioned equation, two current error terms should be considered in the cost function, and defined as the following:

$$g_2 = |i_{d\text{ref}} - i_d(k+1)|^2 + |i_{q\text{ref}} - i_q(k+1)|^2 \tag{32}$$

2) Nonadjacent-Phase Open-Circuit Fault: The stator voltage equation under the phases-B and -E open-circuit fault can be calculated as

$$U_{s2} = R_s I_{s2} + \frac{d}{dt}\left(L_s I_{s2} + \varphi_{s2}^{\text{BE}}\right) \tag{33}$$

where

$$\varphi_{s2}^{\text{BE}} = \begin{bmatrix} \varphi_a \\ \varphi_c \\ \varphi_d \end{bmatrix} = \varphi_m \begin{bmatrix} \cos(\theta) \\ \cos(\theta - 2\alpha) \\ \cos(\theta - 3\alpha) \end{bmatrix}. \tag{34}$$

The motor voltage equation on the synchronous frame can be expressed by

$$\begin{bmatrix} u_d & u_q & u_0 \end{bmatrix} = T_{\text{Park}}^2 T_{\text{Clarke}}^{\text{BE}} \begin{bmatrix} U_a & U_c & U_d \end{bmatrix}^T. \tag{35}$$

Substituting (16) and (17) into (35), the following equation can be obtained

$$\begin{cases} u_d = i_d R_s + L_d \dfrac{di_d}{dt} - \omega_e L_q i_q + e_d \\ u_q = i_q R_s + L_q \dfrac{di_q}{dt} + \omega_e L_d i_d + e_q \\ u_0 = -0.4(e_B + e_E) \end{cases} \tag{36}$$

where e_B and e_E are the back-EMF of the phases B and E, and the calculations of e_d, e_q are detailed in Appendix B-2.

Applying the Euler formula to discretize the voltage equation in (36) and transforming the result into a single time step, the predictive current model can be obtained as

$$\begin{cases} i_d(k+1) = i_d(k) + \dfrac{Ts}{Ld}(u_d(k) - R_s i_d(k) \\ \qquad\qquad + \omega_e L_q i_q(k) - e_d(k)) \\ i_q(k+1) = i_q(k) + \dfrac{Ts}{Lq}(u_q(k) - R_s i_q(k) \\ \qquad\qquad - \omega_e L_d i_d(k) - e_q(k)). \end{cases} \tag{37}$$

From the aforementioned equation, two current error terms should be considered in the cost function, and defined as the following:

$$g_2 = |i_{d\text{ref}} - i_d(k+1)|^2 + |i_{q\text{ref}} - i_q(k+1)|^2. \tag{38}$$

C. Digital Delay Compensation

In real-time implementation, the optimal switching vector that minimizes the cost function is selected, and applied during the next sampling period. The one-step delay between the desired vector and the actual vector caused by digital processing will deteriorate the performance of the system. In this article, a digital delay compensation scheme is employed to compensate this delay [23].

Taking the condition of a single-phase fault as an example, the measured currents and the applied switching state at the *k*th sampling instant are used in (26) to estimate the current values at the (k+1)th sampling instant. Then, these estimated currents are used as the initial prediction values for all available vectors in the defined control set during (k+2)th control interval. The prediction can be realized through one step forward shift of the model, and the improved cost function with the predicted currents during (k+2)th control interval are shown as

$$g_1 = |i_{d\text{ref}} - i_d(k+2)|^2 + |i_{q\text{ref}} - i_q(k+2)|^2 + |i_{z\text{ref}} - i_z(k+2)|^2 \tag{39}$$

$$g_2 = |i_{d\text{ref}} - i_d(k+2)|^2 + |i_{q\text{ref}} - i_q(k+2)|^2. \tag{40}$$

V. Fault-Tolerant Control for MTPA Operation

A. VSIC-MTPA

As a high-performance control method, the VSIC-MTPA has been widely used in the IPMSM drives. In this section, the accuracy of the algorithm [41] will be improved, and the control strategy will be applied to the fault-tolerant operation.

Under the premise of ignoring the iron loss of the motor, the mechanical power of the motor can be expressed as

$$\begin{aligned} P_m &= \frac{5}{2}\left[(u_d - R_s i_d) i_d + (u_q - R_s i_q) i_q\right] \\ &= \frac{5}{2}\left[(u_q - R_s i_q) + \frac{(u_d - R_s i_d)}{i_q} i_d\right] i_q. \end{aligned} \tag{41}$$

And the output torque can be obtained from

$$T_e = \frac{P_m}{\omega_m} = \frac{5}{2}\left[p\varphi_m + p(L_d - L_q) i_d\right] i_q \tag{42}$$

where p is the number of pole pairs, and ω_m is the rotor mechanical speed.

The output torque can be denoted as follows:

$$T_e = \frac{5}{2}\left[\frac{(u_q - R_s i_q)}{\omega_m} + \frac{(u_d - R_s i_d)}{i_q \omega_m} i_d\right] i_q. \tag{43}$$

Comparison of (43) with (42) leads to

$$\begin{cases} \dfrac{(u_q - R_s i_q)}{\omega_m} = p\varphi_m \\ \dfrac{(u_d - R_s i_d)}{i_q \omega_m} = p(L_d - L_q). \end{cases} \tag{44}$$

In [41], a small virtual high-frequency sinusoidal signal $\Delta\beta$ is utilized as the injection angle variation, and the $\Delta\beta$ can be expressed as

$$\Delta\beta = A\sin(\omega_h t) \tag{45}$$

where *A* is the amplitude of the injection signal, and ω_h is the frequency of the injection signal. The electromagnetic torque after high-frequency signal injection can be expressed as

$$T_e^h(\beta + A\sin(\omega_h t) = \frac{5}{2}\left[\frac{(u_q - R_s i_q)}{\omega_m} + \frac{(u_d - R_s i_d)}{i_q \omega_m} i_d^h\right] i_q^h \tag{46}$$

where β is the current angle.

According to the voltage equation of the IPMSM in *d–q* coordinates, the current is constant in steady state. Hence, the differential term is zero and the equation can be expressed as

$$\begin{cases} u_d = L_d \dfrac{di_d}{dt} - p\omega_m L_q i_q + R_s i_d = -p\omega_m L_q i_q + R_s i_d \\ u_q = L_q \dfrac{di_q}{dt} + p\omega_m \varphi_m + p\omega_m L_d i_d + R_s i_q = p\omega_m \varphi_m \\ \qquad\qquad + p\omega_m L_d i_d + R_s i_q. \end{cases} \tag{47}$$

From (47), the following relationship can be obtained:

$$\begin{cases} \dfrac{(u_d - R_s i_d)}{i_q \omega_m} = -pL_q \\ \dfrac{(u_q - R_s i_q)}{\omega_m} = pL_d i_d + p\varphi_m. \end{cases} \tag{48}$$

Substituting (48) into (46), the following equation can be obtained:

$$T_e^h = \frac{5}{2}\left[p\varphi_m + pL_d i_d - pL_q i_d^h\right] i_q^h. \tag{49}$$

Fig. 6. Schematic of virtual signal injection block.

In (49), the high-frequency signal is not fully injected, and the correct expression of the torque containing the high frequency signal should be written as follows:

$$T_e^h = \frac{5}{2}\left[p\varphi_m + pL_d i_d^h - pL_q i_d^h\right] i_q^h. \tag{50}$$

Substituting (44) into (50), the following equation can be obtained:

$$T_e^h = \frac{5}{2}\left[\frac{(u_q - R_s i_q)}{\omega_m} - pL_d i_d + \frac{(u_d - R_s i_d)}{i_q \omega_m} i_d^h + pL_d i_d^h\right] i_q^h. \tag{51}$$

Assuming that (51) is a function of $\Delta\beta$ and it can be transformed by Taylor's series expansion as follows:

$$\begin{aligned} T_e^h(\beta + A\sin(\omega_h t) &= T_e(\beta) + \frac{\partial T_e}{\partial \beta} A\sin(\omega_h t) \\ &\quad + \frac{\partial}{\partial \beta}\left(\frac{\partial T_e}{\partial \beta}\right) A^2 \sin^2(\omega_h t) + \cdots \end{aligned} \tag{52}$$

$\partial Te/\partial\beta$ can be extracted from the torque signal T_e^h with the signal processing technique shown in Fig. 6.

A bandpass filter whose center frequency is equal to the frequency of virtually injected signal is utilized to eliminate the higher order term in (52). Its output is multiplied by $\sin(\omega_h t)$, and the result is given as follows:

$$k\frac{\partial T_e}{\partial \beta} A\sin^2(\omega_h t) = \frac{1}{2} kA \frac{\partial T_e}{\partial \beta} - \frac{\partial T_e}{\partial \beta} kA\cos(2\omega_h t) \tag{53}$$

where *k* is the gain of the bandpass filter at ω_h. The right-hand side of (53) will be filtered by a first-order low-pass filter whose cutoff frequency is below the virtually injected signal frequency ω_h and the filter output is proportional to $\partial Te/\partial\beta$.

B. MTPA Fault-Tolerant Control

From (51), the speed, the *d–q* axes voltages, and *d–q* axes currents can be achieved easily for the MTPA operation according to Sections III and IV. The healthy phase currents under the phase-A open-circuit fault can be expressed as

$$\begin{cases} I_b = 1.382I\cos(\theta - 0.2\pi + \beta) \\ I_c = 1.382I\cos(\theta - 0.8\pi + \beta) \\ I_d = 1.382I\cos(\theta + 0.8\pi + \beta) \\ I_e = 1.382I\cos(\theta + 0.2\pi + \beta) \end{cases} \tag{54}$$

where *I* is the amplitude of the fundamental current under normal condition; and β is the current angle. The currents in *d–q* axes (*id*, *iq*) will be controlled to realize the fault-tolerant control for the MTPA operation. i_z has to be controlled to zero to ensure harmonic-free current and ripple-free torque operation when the open-circuit fault occurs [6].

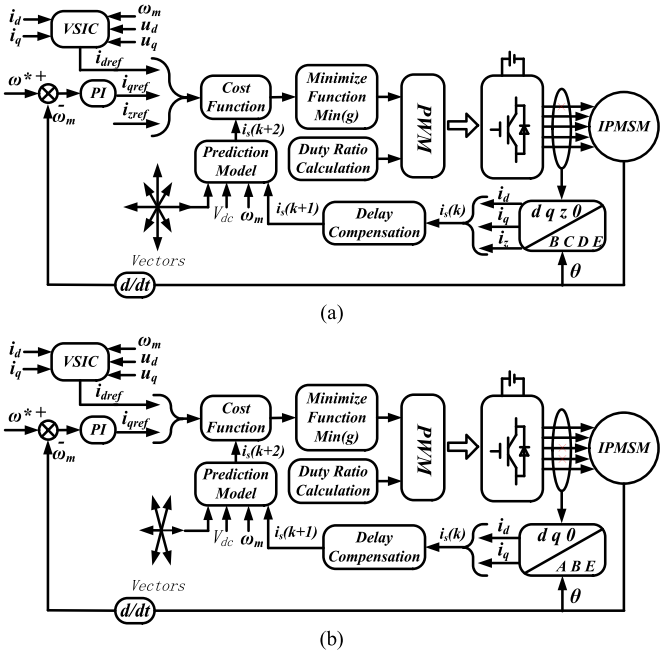

Fig. 7. FCS-MPC-based fault-tolerant control scheme for the five-phase IPMSM. (a) Phase-A open-circuit fault. (b) Phases-C and -D open-circuit fault.

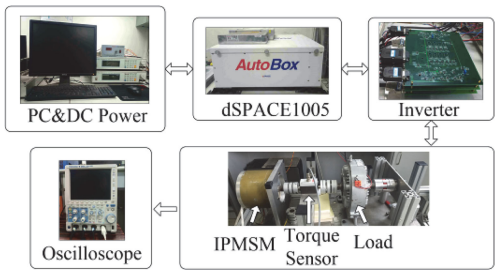

Fig. 8. Experimental platform.

Similarly, the healthy phase currents under the phases-CD and -BE open circuit can also be expressed, respectively, as follows:

$$\begin{cases} I_a = 3.618I\cos(\theta+\beta) \\ I_b = 2.236I\cos(\theta-0.8\pi+\beta) \\ I_e = 2.236I\cos(\theta+0.8\pi+\beta) \end{cases} \tag{55}$$

$$\begin{cases} I_a = 1.382I\cos(\theta+\beta) \\ I_c = 2.236I\cos(\theta-0.6\pi+\beta) \\ I_d = 2.236I\cos(\theta+0.6\pi+\beta). \end{cases} \tag{56}$$

Fig. 7 shows the FCS-MPC-based fault-tolerant control schematic of the five-phase IPMSM under open-circuit faults. The diagram of the VSIC block has been given in Fig. 6.

VI. Experimental Results

In order to validate the proposed fault-tolerant control strategy, an experimental platform has been conducted as shown in Fig. 8. The test platform is based on a 2-kW five-phase IPMSM, The motor with the parameters given in Table V has been designed and built for testing as shown in Fig. 1(a). The proposed fault-tolerant algorithm of the five-phase motor is developed and implemented in the dSPACE1005 controller, and motor torque is measured by a high precision torque sensor (T20WN/20 Nm). The five-phase half-bridge inverter is also shown in Fig. 8. It is important to mention that during the following experimental tests, the frequency of IGBTs is fixed at 10 kHz and the sample rate of the current sensor is 10 kHz. In the experiment, the fault occurrence is emulated by manually disconnecting the cable.

TABLE V
Practical Parameters of Prototype Motor

Parameters	Value
Pole-pairs	4
Fundamental permanent magnet flux linkage	0.111 Wb
Phase resistance	0.8 Ω
Fundamental d-axis inductance	5.3 mH
Fundamental q-axis inductance	17 mH
leakage inductance	0.23 mH
RMS current value	7.67 A
Rated speed	1500 r/min
Rated torque	10 Nm

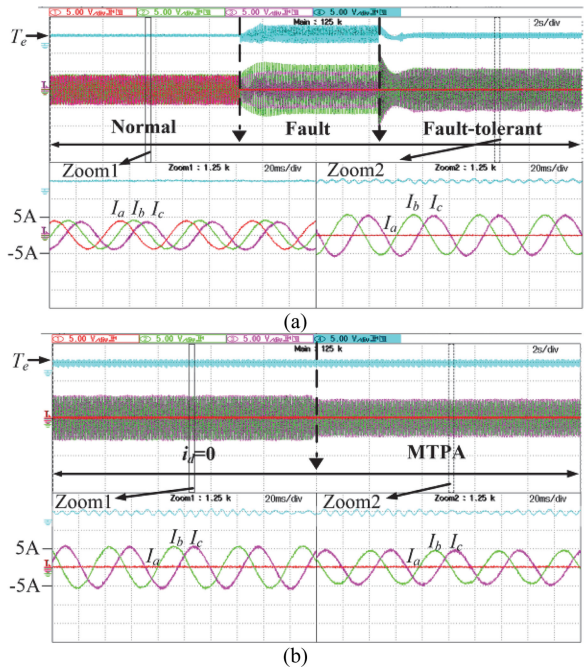

Fig. 9. Torque and currents waveforms under a single-phase fault. (a) Pre- and postfault-tolerant operation with FCS-MPC. (b) $I_d = 0$ to MTPA fault-tolerant operation. T_e is scaled to 10 Nm/div, phase currents are scaled to 5 A/div.

A. Fault-Tolerant Operation Test

The behavior of the proposed fault-tolerant control algorithm during the single-phase fault is first analyzed. The motor is operated at a constant speed of 300 r/min and the load torque is 4.4 Nm. Fig. 9 shows the phase currents and torque waveforms around the fault occurrence. Fig. 9(a) is the process from normal operation to fault and fault-tolerant operation under the FCS-MPC, in which the $i_d = 0$ fault-tolerant control is implemented.

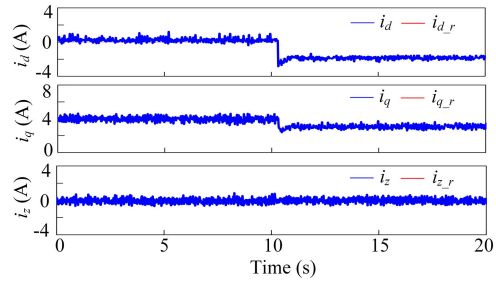

Fig. 10. Waveforms of d–q–z currents from $i_d = 0$ to the MTPA fault-tolerant operation under a single-phase fault.

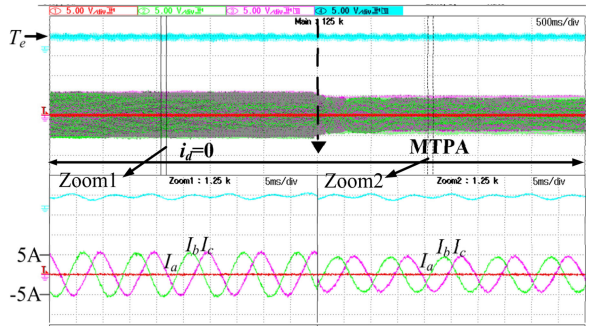

Fig. 11. Torque and currents waveforms from $i_d = 0$ to MTPA fault-tolerant operation under a single-phase fault at the speed of 1500 r/min.

The Zoom1 and Zoom2 shows that the measured torque and currents waveforms under healthy and fault tolerant control. Taking phase B as example, its amplitudes are 4 and 5.6 A in Zoom1 and Zoom2, respectively, which match the theoretical waveforms mentioned previously in Section V-B. Fig. 9(b) shows the torque and currents waveforms from $i_d = 0$ to MTPA operation under the phase-A open-circuit fault. From the Zoom1 and Zoom2, it can be seen that the current amplitudes of the phase B decrease from 5.6 to 5 A.

Fig. 10 shows the corresponding waveforms of d–q–z currents from $i_d = 0$ to MTPA operation under the phase-A open-circuit fault in Fig. 9(b). In $i_d = 0$ control, the i_q can be calculated to be 4 A, and the torque is about 4.4 Nm. In the MTPA operation, the MTPA point is about 30°, the i_d and i_q are –1.9 and 3.2 A, respectively. In this case, the calculated torque is 4.3 Nm. Thus, it can be concluded that the MTPA fault-tolerant control can obtain the same torque with less stator phase currents. Besides, the system has a good steady state before and after the algorithm switching.

Fig. 11 shows the experimental result under the rated speed of 1500 r/min, taking phase B as reference, its amplitude decrease from 5.6 to 5 A, which shows that the proposed method can achieve an ideal results at a high speed.

To verify the control accuracy of the proposed control strategy, Fig. 12 shows a contrastive tracking experimental result of MTPA points with the control method in [41] under the fault-tolerant condition. For a given torque command, tests are performed by varying the current angle while the magnitude of the current keeps constant. The MTPA point shown in Fig. 12

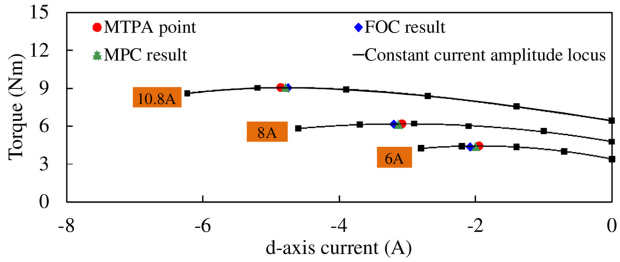

Fig. 12. FOC-MTPA and MPC-MTPA tracking experimental results under a single-phase fault.

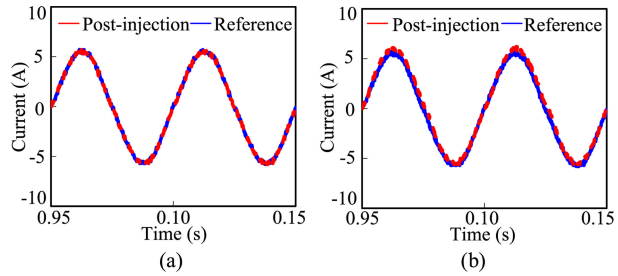

Fig. 13. Waveforms of current using (a) VSIC-MTPA and (b) SVIC -MTPA.

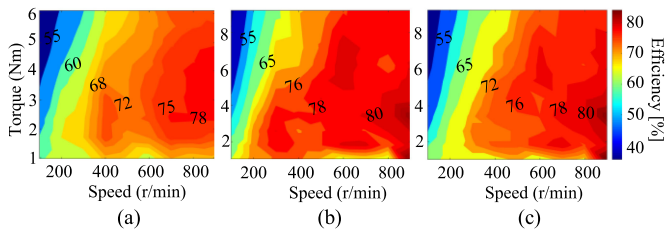

Fig. 14. Efficiency maps under the phase-A open-circuit fault using (a) $i_d = 0$ fault-tolerant control method with MPC, (b) MTPA fault-tolerant method with MPC, and (c) MTPA fault-tolerant method with FOC.

represents the actual MTPA points under different current amplitudes. The FOC result represents the MTPA point found by the FOC-MTPA control [41], the MPC result represents the MTPA point found by the proposed control method. As shown in Fig. 12, two control methods can realize highly accurate tracking of MTPA points under the fault-tolerant condition, and the accuracy of the proposed control method is relatively high.

Fig. 13 shows a comparison between the proposed MTPA method and a space vector signal injection (SVSI) MTPA in [38], which injects a real signal into motor. It is obvious that the current under the latter method contains harmonics caused by the real signal. Fig. 14 shows the efficiency map under the phase-A open-circuit fault-tolerant operation, which is measured by the YOKOGAWA WT1800 power analyzer and torque transducer. The power analyzer is chosen as the 1P2W wiring setting to measure the electrical input power of the healthy phases separately, and then, the total input power is obtained by adding them together. The output power is calculated by the measured torque and the measured speed. The maximum output torques are limited by the amplitude of the phase current (10.8 A).

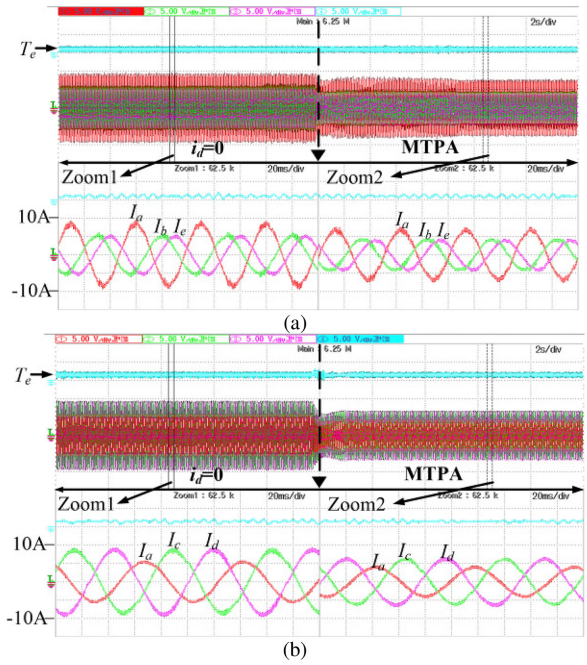

Fig. 15. Torque and currents waveforms from $i_{\mathrm{d}} = 0$ to MTPA fault-tolerant operation under a double-phase fault. (a) Phases-C and -D open circuit. (b) Phases-B and -E open circuit. *Te* is scaled to 10 Nm/div, phase currents are scaled to 5 A/div.

The speed range is from 100 to 900 r/min, and the maximum speed is limited by the dc voltage. Fig. 14(a) and (b) are efficiency maps using the proposed FCS-MPC method, which show that the output torque capability and operation efficiency with the same current limitation is higher under the MTPA fault-tolerant operation. Fig. 14(c) shows the efficiency map using the FOC fault-tolerant control method in [41]. It can be seen that the proposed method offers higher efficiency under the same load limitation.

Fig. 15 exhibits the torque and currents waveforms from $i_d = 0$ to the MTPA fault-tolerant operation under the double-phase fault. The experimental results under adjacent-phase (phases C and D) fault have been shown in Fig. 15(a). The reference speed is set as 300 r/min and the load torque is set as 2.5 Nm. Taking phase A as reference, its amplitudes are 9.2 and 7.4 A under $i_d = 0$ and MTPA operation, respectively. Fig. 15(b) shows the experimental results under nonadjacent-phase (phases B and E) fault. The reference speed is set as 300 r/min and the load torque is set as 3.7 Nm. Taking phase C as reference, its amplitudes are 9.4 and 6.6 A under two control algorithms, respectively. Also, the magnified healthy phase currents in Zooms show that the measured healthy currents waveforms match the theoretical waveforms mentioned previously in Section V-B.

B. Dynamic Performances of Fault-Tolerant Operation

To evaluate the dynamic response of the proposed fault-tolerant control, several tests have been performed and compared with FOC-based fault-tolerant control for MTPA operation [41] under different fault conditions.

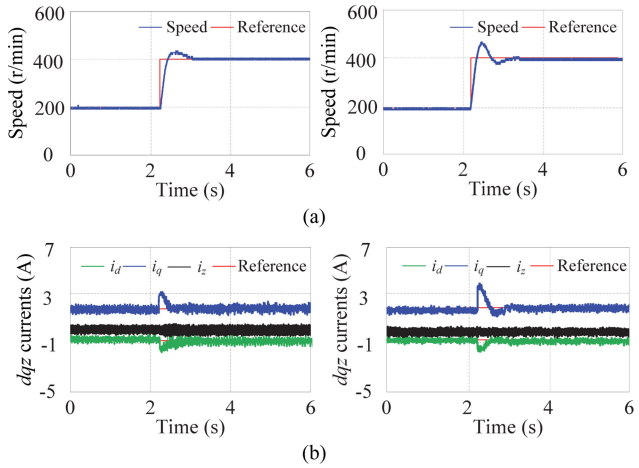

Fig. 16. Speed step under the phase-A open-circuit fault using MPC-MTPA (left) and FOC-MTPA (right). (a) Speed response. (b) *d–q–z* currents response.

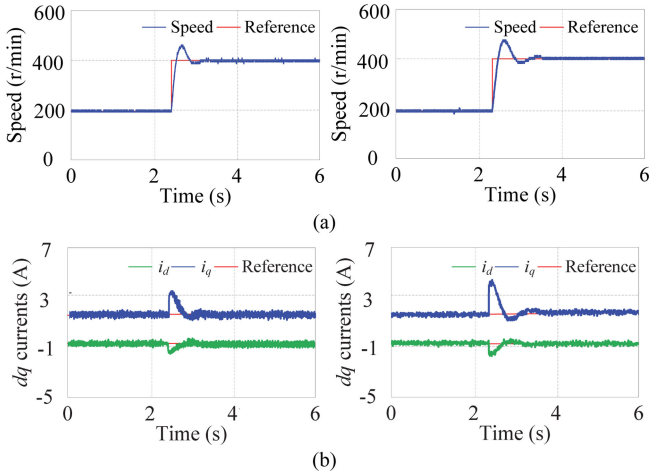

Fig. 17. Speed step tests under phases-C and -D open-circuit fault using MPC-MTPA (left) and FOC-MTPA (right). (a) Speed response. (b) *d–q* currents response.

Fig. 16 shows the experimental speed and *d–q–z* currents response under a speed step. The reference speed is varied from 200 to 400 r/min. It can be observed that the responses of the speed and *d–q–z* currents under the phase-A open-circuit fault are almost same. The speed tracking is satisfactorily achieved with a fast response and low overshoot. The *d–q–z* currents reference is quickly modified during the acceleration transients in order to provide fast dynamics, whereas the *d–q–z* currents are kept constant during the test confirming the control decoupling. Although the two control strategies drive the motor in a similar way during the tests, the overshoot of the speed in the case of MPC-MTPA control is about 5%, and the settling time is about 0.8 s; the overshoot of the speed with the FOC-MTPA is about 12.5%, and the settling time is about 1 s. Consequently, the proposed method provides faster dynamic response and lower overshoot than FOC-MTPA at the expense of a higher current ripple. The fact also holds true in the double-phase fault condition, as shown in Fig. 17. As expected, the *z* current is kept

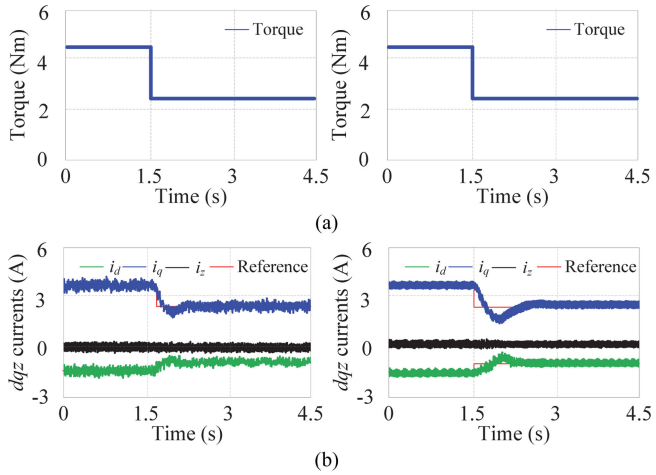

Fig. 18. Load step tests under phase-A open-circuit fault using MPC-MTPA (left) and FOC-MTPA (right). (a) Torque response. (b) *d–q–z* currents response.

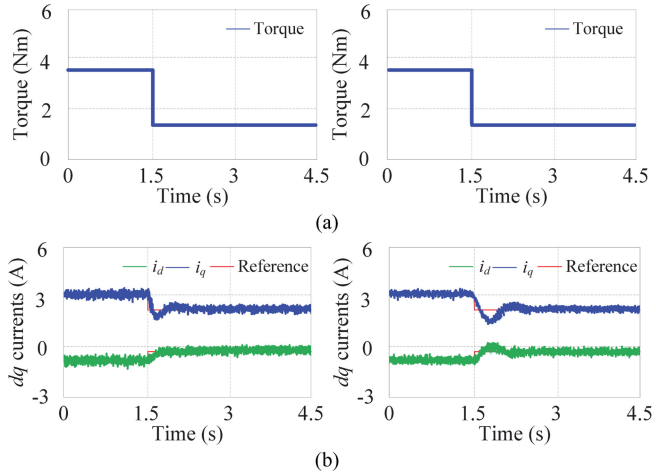

Fig. 19. Load step tests under phases-C and -D open-circuit fault using MPC-MTPA (left) and FOC-MTPA (right). (a) Torque response. (b) *d–q* currents response.

close to zero all throughout the test, thus, proving to remain unaffected in dynamic conditions.

Fig. 18 shows a test to further verify that the proposed strategy maintains a high performance and robustness in terms of load step. The motor is driven in steady state with constant speed of 300 r/min. The transient states consist in applying to the motor one-step transitions of the load from 4.5 to 2.5 Nm. Obtained results show that both control methods offer nearly the same performance, the *d–q* currents always keep a corresponding relationship and the *z* current is kept close to zero in the process of torque change. Also they can track the given reference value with a small overshoot. Compared with [41], the proposed method provides faster control response and superior performance. It also holds true in the double-phase fault condition, as shown in Fig. 19.

A qualitative comparative analysis is summarized in Table VI. The experimental results show that both control methods can maintain the safe operation under the fault condition, but the proposed method provides a higher MTPA point tracking accuracy and operation efficiency, also, the speed and torque response are faster than the method in [41] at the expense of a higher current ripple.

TABLE VI
QUALITATIVE COMPARISON BETWEEN THE MPC-MTPA AND FOC-MTPA METHODS UNDER THE OPEN-CIRCUIT FAULT OPERATION

System performance	MPC-MTPA	FOC-MTPA
MTPA point tracking error	Negligible	Slight
Efficiency	Excellent	Good
Overshoot of speed and *dq* currents under speed step	Slight	Low
Overshoot of *dq* currents under load step	Slight	Low
Settling time of speed and *dq* currents under speed step	Fast	General
Settling time of *dq* currents under load step	Fast	General
Current ripple	General	Good

VII. CONCLUSION

This article proposes a novel fault-tolerant control strategy based on the FCS-MPC for the IPMSM drives under different fault conditions. The reduced-order transformation matrices for fault conditions have been derived first to construct the distributions of space voltage vectors, and the fundamental decoupled models of the five-phase IPMSM under the open-circuit fault are obtained. Then, the FCS-MPC-based fault-tolerant method has been proposed, which can enhance the torque waveform quality, reduce the harmonic components of phase currents, and keep low amount of computation for the driving system. Based on the decoupled models and computing method, the VSIC has been applied to realize the MTPA fault-tolerant operation by postfault FCS-MPC under open-circuit faults, which can reduce the amplitudes of the phase currents and improve the efficiency of the system. The experimental results have been offered to verify the validity of the proposed method in postfault tolerant operation, which provide the satisfactory steady and dynamic performances.

APPENDIX

A. Single-Phase Open-Circuit Fault

$$\begin{bmatrix} e_d \\ e_q \\ e_z \\ e_0 \end{bmatrix} = T^1_{\text{Park}} T^A_{\text{Clarke}} \frac{d\varphi^A_{s1}}{dt} = T^1_{\text{Park}} T^A_{\text{Clarke}} \cdot \omega_e \varphi_m \begin{bmatrix} -\sin(\theta-\alpha) \\ -\sin(\theta-2\alpha) \\ -\sin(\theta-3\alpha) \\ -\sin(\theta-4\alpha) \end{bmatrix} \quad (1)$$

where

$$T^1_{\mathrm{Park}}T^A_{\mathrm{Clarke}}\begin{bmatrix}-\sin(\theta-\alpha)\\-\sin(\theta-2\alpha)\\-\sin(\theta-3\alpha)\\-\sin(\theta-4\alpha)\end{bmatrix}=T^1_{\mathrm{Park}}\begin{bmatrix}-0.5\sin(\theta)\\0.9471\cos(\theta)\\0.1382\cos(\theta)\\\sin(\theta)\end{bmatrix}$$
$$=\begin{bmatrix}0.4471\sin(\theta)\cos(\theta)\\0.4471\cos^2(\theta)+0.5\\0.1382\cos(\theta)\\\sin(\theta)\end{bmatrix}.$$

B. Double-Phase Open-Circuit Fault

1) Adjacent-Phase Open-Circuit Fault:

$$\begin{bmatrix}e_d\\e_q\\e_0\end{bmatrix}=T^2_{\mathrm{Park}}T^{\mathrm{CD}}_{\mathrm{Clarke}}\frac{d\varphi^{\mathrm{CD}}_{s2}}{dt}=T^2_{\mathrm{Park}}T^{\mathrm{CD}}_{\mathrm{Clarke}}$$
$$\cdot\,\omega_e\varphi_m\begin{bmatrix}-\sin(\theta)\\-\sin(\theta-\alpha)\\-\sin(\theta-4\alpha)\end{bmatrix}\tag{2}$$

where

$$T^2_{\mathrm{Park}}T^{\mathrm{CD}}_{\mathrm{Clarke}}\begin{bmatrix}-\sin(\theta)\\-\sin(\theta-\alpha)\\-\sin(\theta-4\alpha)\end{bmatrix}$$
$$=0.4T^2_{\mathrm{Park}}\begin{bmatrix}-0.3183\sin(\theta)\\1.809\cos(\theta)\\-1.618\sin(\theta)\end{bmatrix}$$
$$=0.4\begin{bmatrix}1.4907\sin(\theta)\cos(\theta)\\1.4907\cos^2(\theta)+0.3183\\-1.618\sin(\theta)\end{bmatrix}.$$

2) Nonadjacent-Phase Open-Circuit Fault:

$$\begin{bmatrix}e_d\\e_q\\e_0\end{bmatrix}=T^2_{\mathrm{Park}}T^{\mathrm{BE}}_{\mathrm{Clarke}}\frac{d\varphi^{\mathrm{BE}}_{s2}}{dt}=T^2_{\mathrm{Park}}T^{\mathrm{BE}}_{\mathrm{Clarke}}$$
$$\cdot\,\omega_e\varphi_m\begin{bmatrix}-\sin(\theta)\\-\sin(\theta-2\alpha)\\-\sin(\theta-3\alpha)\end{bmatrix}\tag{3}$$

where

$$T^2_{\mathrm{Park}}T^{\mathrm{BE}}_{\mathrm{Clarke}}\begin{bmatrix}-\sin(\theta)\\-\sin(\theta-2\alpha)\\-\sin(\theta-3\alpha)\end{bmatrix}$$
$$=0.4T^2_{\mathrm{Park}}\begin{bmatrix}-2.1817\sin(\theta)\\0.691\cos(\theta)\\0.618\sin(\theta)\end{bmatrix}$$
$$=0.4\begin{bmatrix}-1.4907\sin(\theta)\cos(\theta)\\-1.4907\cos^2(\theta)+2.1817\\0.618\sin(\theta)\end{bmatrix}.$$

REFERENCES

[1] E. Levi, F. Barrero, and M. J. Duran, "Multiphase machines and drives—Revisited," *IEEE Trans. Ind. Electron.*, vol. 63, no. 1, pp. 429–432, Jan. 2016.

[2] F. Barrero and M. J. Duran, "Recent advances in the design, modeling and control of multiphase machines—Part I," *IEEE Trans. Ind. Electron.*, vol. 63, no. 1, pp. 449–458, Jan. 2016.

[3] M. J. Duran and F. Barrero, "Recent advances in the design, modeling and control of multiphase machines—Part II," *IEEE Trans. Ind. Electron.*, vol. 63, no. 1, pp. 459–468, Jan. 2016.

[4] G. Liu, L. Qu, W. Zhao, Q. Chen, and Y. Xie, "Comparison of two SVPWM control strategies of five-phase fault-tolerant permanent-magnet motor," *IEEE Trans. Power Electron.*, vol. 31, no. 9, pp. 6621–6630, Sep. 2016.

[5] Q. Chen, G. Liu, W. Zhao, L. Qu, and G. Xu, "Asymmetrical SVPWM fault-tolerant control of five-phase PM brushless motors," *IEEE Trans. Energy Convers.*, vol. 32, no. 1, pp. 12–22, Mar. 2017.

[6] H. Zhou, W. Zhao, G. Liu, R. Cheng, and Y. Xie, "Remedial field-oriented control of five-phase fault-tolerant permanent-magnet motor by using reduced-order transformation matrices," *IEEE Trans. Ind. Electron.*, vol. 64, no. 1, pp. 169–178, Jan. 2017.

[7] I. González-Prieto, M. J. Duran, and F. J. Barrero, "Fault-tolerant control of six-phase induction motor drives with variable current injection," *IEEE Trans. Power Electron.*, vol. 32, no. 10, pp. 7894–7903, Oct. 2017.

[8] M. Bermudez, I. Gonzalez-Prieto, F. Barrero, H. Guzman, M. J. Duran, and X. Kestelyn, "Open-phase fault-tolerant direct torque control technique for five-phase induction motor drives," *IEEE Trans. Ind. Electron.*, vol. 64, no. 2, pp. 902–911, Feb. 2017.

[9] M. Bermudez, I. Gonzalez-Prieto, F. Barrero, H. Guzman, X. Kestelyn, and M. J. Duran, "An experimental assessment of open-phase fault-tolerant virtual-vector-based direct torque control in five-phase induction motor drives," *IEEE Trans. Power Electron.*, vol. 33, no. 3, pp. 2774–2784, Mar. 2018.

[10] P. G. Entrambasaguas, I. Gonzalez-Prieto, M. J. Duran, M. Bermudez, and F. Barrero, "Fault tolerance in direct torque control with virtual voltage vectors," *Rev. Iberoam. Autom. Inform. Ind.*, vol. 16, no. 1, pp. 56–65, 2019.

[11] Y. Z. Zhou, X. G. Lin, and M. Cheng, "A fault-tolerant direct torque control for six-phase permanent magnet synchronous motor with arbitrary two opened phases based on modified variables," *IEEE Trans. Energy Convers.*, vol. 31, no. 2, pp. 549–556, Jun. 2016.

[12] K. D. Hoang, Z. Q. Zhu, and M. Foster, "Direct torque control of permanent magnet brushless AC drive with single-phase open-circuit fault accounting for influence of inverter voltage drop," *IET Elec. Power Appl.*, vol. 7, no. 5, pp. 369–380, May 2013.

[13] L. Zhang, Y. Fan, R. Cui, R. D. Lorenz, and M. Cheng, "Fault-tolerant direct torque control of five-phase FTFSCW-IPM motor based on analogous three-phase SVPWM for electric vehicle applications," *IEEE Trans. Veh. Technol.*, vol. 67, no. 2, pp. 910–919, Feb. 2018.

[14] A. Tani, M. Mengoni, L. Zarri, G. Serra, and D. Casadei, "Control of multiphase induction motors with an odd number of phases under open circuit phase faults," *IEEE Trans. Power Electron.*, vol. 27, no. 2, pp. 565–577, Feb. 2012.

[15] A. K. M. Arafat and S. Choi, "Optimal phase advance under fault-tolerant control of a five-phase permanent magnet assisted synchronous reluctance motor," *IEEE Trans. Ind. Electron.*, vol. 65, no. 4, pp. 2915–2924, Apr. 2018.
[16] A. K. M. Arafat and S. Choi, "Active current harmonic suppression for torque ripple minimization at open-phase faults in a five-phase PMa-SynRM," *IEEE Trans. Ind. Electron.*, vol. 66, no. 2, pp. 922–931, Feb. 2019.
[17] B. Tian, Q. An, J. Duan, D. Sun, L. Sun, and D. Semenov, "Decoupled modeling and nonlinear speed control for five-phase PM motor under single-phase open fault," *IEEE Trans. Power Electron.*, vol. 32, no. 7, pp. 5473–5486, Jul. 2017.
[18] B. Tian, Q. An, J. Duan, D. Semenov, D. Sun, and L. Sun, "Cancellation of torque ripples with FOC strategy under two-phase failures of the five-phase PM motor," *IEEE Trans. Power Electron.*, vol. 32, no. 7, pp. 5459–5472, Jul. 2017.
[19] C. Lim, E. Levi, M. Jones, N. Abd Rahim, and W. Hew, "FCS-MPC-based control of a five-phase induction motor and its comparison with PI-PWM control," *IEEE Trans. Ind. Electron.*, vol. 61, no. 1, pp. 149–163, Jan. 2014.
[20] T. Geyer and D. E. Quevedo, "Performance of multistep finite control set model predictive control for power electronics," *IEEE Trans. Power Electron.*, vol. 30, no. 3, pp. 1633–1644, Mar. 2015.
[21] H. Guzman *et al.*, "Comparative study of predictive and resonant controllers in fault-tolerant five-phase induction motor drives," *IEEE Trans. Ind. Electron.*, vol. 63, no. 1, pp. 606–617, Jan. 2016.
[22] F. Mwasilu, E. Kim, M. S. Rafaq, and J. Jung, "Finite-set model predictive control scheme with an optimal switching voltage vector technique for high-performance IPMSM drive applications," *IEEE Trans. Ind. Electron.*, vol. 14, no. 9, pp. 3840–3848, Sep. 2018.
[23] C. Xue, W. Song, X. Wu, and X. Feng, "A constant switching frequency finite-control-set predictive current control scheme of a five-phase inverter with duty-ratio optimization," *IEEE Trans. Power Electron.*, vol. 33, no. 4, pp. 3583–3594, Apr. 2018.
[24] F. Barrero, M. R. Arahal, R. Gregor, S. Toral, and M. J. Duran, "A proof of concept study of predictive current control for VSI-driven asymmetrical dual three-phase AC machines," *IEEE Trans. Ind. Electron.*, vol. 56, no. 6, pp. 1937–1954, Jun. 2009.
[25] S. Bolognani, S. Bolognani, L. Peretti, and M. Zigliotto, "Design and implementation of model predictive control for electrical motor drives," *IEEE Trans. Ind. Electron.*, vol. 56, no. 6, pp. 1925–1936, Jun. 2009.
[26] I. Gonzalez-Prieto, M. J. Duran, J. J. Aciego, C. Martin, and F. Barrero, "Model predictive control of six-phase induction motor drives using virtual voltage vectors," *IEEE Trans. Ind. Electron.*, vol. 65, no. 1, pp. 27–37, Jan. 2018.
[27] C. Xiong, H. Xu, T. Guan, and P. Zhou, "A constant switching frequency multiple vector based model predictive current control of five-phase PMSM with non-sinusoidal back-EMF," *IEEE Trans. Ind. Electron.*, 2019, to be published, doi: 10.1109/TIE.2019.2907502.
[28] Y. Zhang, D. Xu, J. Liu, S. Gao, and W. Xu, "Performance improvement of model-predictive current control of permanent magnet synchronous motor drives," *IEEE Trans. Ind. Appl.*, vol. 53, no. 4, pp. 3683–3695, Jul./Aug. 2017.
[29] G. Li, J. Hu, Y. Li, and J. Zhu, "An improved model predictive direct torque control strategy for reducing harmonic currents and torque ripples of five phase permanent magnet synchronous motors," *IEEE Trans. Ind. Electron.*, vol. 66, no. 8, pp. 5820–5829, Aug. 2019.
[30] H. Lu, J. Li, R. Qu, D. Ye, and Y. Lu, "Fault-tolerant predictive control of six-phase PMSM drives based on pulse-width-modulation," *IEEE Trans. Ind. Electron.*, vol. 66, no. 7, pp. 4992–5003, Jul. 2019.
[31] Y. Luo and C. Liu, "Pre- and post-fault tolerant operation of a six-phase PMSM motor using FCS-MPC without controller reconfiguration," *IEEE Trans. Veh. Technol.*, vol. 68, no. 1, pp. 254–263, Jan. 2019.
[32] I. Gonzalez-Prieto, M. J. Duran, M. Bermudez, F. Barrero, and C. Martin, "Assessment of virtual-voltage-based model predictive controllers in six-phase drives under open-phase faults," *IEEE J. Emerg. Sel. Topics Power Electron.*, to be published, doi: 10.1109/JESTPE.2019.2915666.
[33] H. Guzman, M. J. Duran, F. Barrero, B. Bogado, and S. Toral, "Speed control of five-phase induction motors with integrated open-phase fault operation using model-based predictive current control techniques," *IEEE Trans. Ind. Electron.*, vol. 61, no. 9, pp. 4474–4484, Sep. 2014.
[34] H. Guzman, F. Barrero, and M. J. Duran, "IGBT-gating failure effect on a fault-tolerant predictive current-controlled five-phase induction motor drive," *IEEE Trans. Ind. Electron.*, vol. 62, no. 1, pp. 15–20, Jan. 2015.
[35] W. Huang, W. Hua, F. Chen, F. Yin, and J. Qi, "Model predictive current control of open-circuit fault-tolerant five-phase flux-switching permanent magnet motor drives," *IEEE J. Emerg. Sel. Topics Power Electron.*, vol. 6, no. 4, pp. 1840–1849, Dec. 2018.
[36] Y. R. Mohamed and T. K. Lee, "Adaptive self-tuning MTPA vector controller for IPMSM drive system," *IEEE Trans. Ind. Electron.*, vol. 21, no. 3, pp. 636–644, Jan. 2006.
[37] S. Jung, J. Hong, and K. Nam, "Current minimizing torque control of the IPMSM using Ferrari's method," *IEEE Trans. Power Electron.*, vol. 28, no. 12, pp. 5603–5617, Dec. 2013.
[38] G. Liu, J. Wang, W. Zhao, and Q. Chen, "A novel MTPA control strategy for IPMSM drives by space vector signal injection," *IEEE Trans. Ind. Electron.*, vol. 64, no. 12, pp. 9243–9252, Dec. 2017.
[39] Q. Tang, A. Shen, P. Luo, H. Shen, W. Li, and X. He, "IPMSMs sensorless MTPA control based on virtual q-axis inductance by using virtual high frequency signal injection," *IEEE Trans. Ind. Electron.*, to be published, doi: 10.1109/TIE.2018.2890487.
[40] J. Wang *et al.*, "An accurate virtual signal injection control of MTPA for an IPMSM with fast dynamic response," *IEEE Trans. Power Electron.*, vol. 33, no. 9, pp. 7916–7926, Sep. 2018.
[41] Q. Chen, W. Zhao, G. Liu, and Z. Lin, "Extension of virtual-signal-injection-based MTPA control for five-phase IPMSM into fault-tolerant operation," *IEEE Trans. Ind. Electron.*, vol. 66, no. 2, pp. 944–955, Feb. 2019.
[42] Q. Chen, G. Xu, G. Liu, W. Zhao, L. Liu, and Z. Lin, "Torque ripple reduction in five-phase IPM motors by lowering interactional MMF," *IEEE Trans. Ind. Electron.*, vol. 65, no. 11, pp. 8520–8531, Nov. 2018.

Guohai Liu (M'07–SM'15) received the B.Sc. degree from Jiangsu University, Zhenjiang, China, in 1985, and the M.Sc. and Ph.D. degrees in electrical engineering and control engineering from Southeast University, Nanjing, China, in 1988 and 2002, respectively.

He has been with Jiangsu University since 1988, where he is currently a Professor and the Dean with the School of Electrical Information Engineering. From 2003 to 2004, he was a Visiting Professor with the Department of Electronic and Electrical Engineering, University of Sheffield, Sheffield, U.K. His teaching and research interests include electrical machines, motor drives for electric vehicles, and intelligent control. He has authored or coauthored more than 200 technical papers and 4 textbooks, and holds 30 patents in these areas.

Dr. Liu is a Fellow of the IET.

Chengyan Song received the B.Sc. degree in control engineering from Jiangsu University, Zhenjiang, China, in 2017, where he is currently working toward the M.Sc. degree in control engineering.

His current research interests include power-electric control of electric machines and fault-tolerant control.

Qian Chen (M'16) received the B.Sc. and Ph.D. degrees in electrical engineering and control engineering from Jiangsu University, Zhenjiang, China, in 2009 and 2015, respectively.

He has been with Jiangsu University since 2015, where he is currently an Associate Professor with the School of Electrical Information Engineering. His current research interests include electric machine design, modeling, fault analysis, and intelligent control.